



1 **Two years of satellite-based carbon dioxide emission quantification at the world's**
2 **largest coal-fired power plants**

3 Daniel H. Cusworth^{1,2}, Andrew K. Thorpe³, Charles E. Miller³, Alana K. Ayasse¹, Ralph Jiorle¹,
4 Riley M. Duren^{1,2,3}, Ray Nassar⁴, Jon-Paul Mastrogiacono⁵, and Robert R. Nelson³

5 ¹Carbon Mapper, Pasadena, CA, USA

6 ²Arizona Institutes for Resilience, University of Arizona, Tucson, AZ, USA

7 ³Jet Propulsion Laboratory, California Institute of Technology, Pasadena, CA, USA

8 ⁴Environment & Climate Change Canada

9 ⁵University of Toronto

10

11 Corresponding Author: Daniel H. Cusworth (dan@carbonmapper.org)

12

13 **Abstract**

14 Carbon dioxide (CO₂) emissions from combustion sources are uncertain in many places
15 across the globe. Satellites have the ability to detect and quantify emissions from large CO₂ point
16 sources, including coal-fired power plants. In this study, we tasked the PRecursores IperSpettrale della
17 Missione Applicativa (PRISMA) satellite imaging spectrometer and the Orbiting Carbon
18 Observatory-3 (OCO-3) instrument onboard the International Space Station at over 30 coal-fired
19 power plants routinely between 2021-2022. CO₂ plumes were detected in 50% of acquired PRISMA
20 scenes, which is consistent with the combined influence of viewing parameters on detection (solar
21 illumination, surface reflectance) and unknown factors (like daily operational status). We compare
22 satellite-derived emission rates to *in situ* stack emission observations and find average agreement to
23 within 27% for PRISMA and 30% for OCO-3, though more observations are needed to robustly
24 characterize the error. We highlight two examples of fusing PRISMA with OCO-2 and OCO-3
25 observations in South Africa and India. For India, we acquired PRISMA and OCO-3 observations on



26 the same day and use the high spatial resolution capability of PRISMA (30 m spatial/pixel resolution)
27 to partition relative contributions of two distinct emitting power plants to the net emission. Though
28 an encouraging start, two years of tasking these satellites did not produce sufficient observations to
29 estimate annual average emission rates within low (<15%) uncertainties. However, as the
30 constellation of CO₂-observing satellites is poised to significantly improve in the coming decade, this
31 study offers an approach to leverage multiple observation platforms to better understand large
32 anthropogenic emission sources.

33

34 **1 Introduction**

35 Anthropogenic carbon dioxide (CO₂) emissions are dominated by strong discrete point
36 sources that result from energy generation at energy supply facilities (e.g., power plants) and
37 industrial facilities (Crippa et al., 2019). Fossil fuel combustion is the largest contributor to warming
38 trends globally since the pre-industrial era (IPCC, 2021). However, there remains uncertainty in the
39 total magnitude of emissions from these sectors as bottom-up emission estimates rely on reported
40 emission factors and activity data, which may vary in granularity and quality across countries and
41 provinces (Hong et al., 2017; Guan et al., 2017). Accurate CO₂ emission quantification is important
42 in light of the Paris Agreement, as participating countries must develop plans and report progress to
43 reduce their country's greenhouse gas (GHG) emissions (UN, 2015). Leveraging atmospheric
44 measurements, particularly satellite remote sensing, can help reduce uncertainty in facility-level CO₂
45 emission estimates, provided that the observations are accurate and sufficiently sample the facility in
46 time (Hill and Nassar, 2019). Deployed systematically with robust error characterization, this system
47 could be an anchor towards assessing and verifying anticipated CO₂ emission reductions as part of
48 national and global GHG emission reduction plans and agreements.



49 Several studies have shown that atmospheric sounding satellites can accurately quantify some
50 point source CO₂ emissions from large individual coal-fired power plants. First, the Orbiting Carbon
51 Observatory-2 (OCO-2; Crisp et al., 2017) is a space-based instrument that observes solar
52 backscattered near-infrared radiance in the oxygen A band (758-772 nm; 0.04 nm spectral resolution),
53 the weak CO₂ band (1594-1619 nm; 0.08 nm spectral resolution), and strong CO₂ band (2042-2082
54 nm; 0.10 nm spectral resolution). OCO-2 views in nadir mode over land, while sun glint mode
55 increases the signal over water giving measurements both land and water, and target mode to target
56 specific validation or calibration sites. With its 10-km wide swath, $\leq 1.3 \times 2.25$ km² pixel resolution,
57 and better than 1.0 ppm precision for retrievals of the column-mean dry-air mole fraction of CO₂
58 (XCO₂) (Taylor et al., 2023), OCO-2 is sensitive to single CO₂ point sources that emit sufficiently
59 close to an OCO-2 orbital track and are spatially isolated from other major CO₂ sources. Using
60 satellite observations from OCO-2, Nassar et al. (2017) detected strong CO₂ enhancements in the
61 near vicinity of seven large coal-fired power plants and employed a Gaussian plume model emission
62 quantification technique to estimate emission rates for these facilities. Further study expanded the set
63 of facilities that could be quantified by OCO-2 (Nassar et al., 2021). Other studies have leveraged
64 the nitrogen dioxide (NO₂) retrieval capability and wide swath of the TROPOspheric Monitoring
65 Instrument (TROPOMI; van Geffen et al., 2020) to attribute and corroborate strong CO₂ signals seen
66 in OCO-2 observations (Hakkarainen et al., 2021; Reuter et al., 2019). The Orbiting Carbon
67 Observatory-3 (OCO-3; Eldering et al., 2019), the flight spare of OCO-2, has been on board the
68 International Space Station (ISS) since May 2019. Like OCO-2, it has been shown capable of
69 quantifying CO₂ power plant emissions. Nassar et al. (2022) analyzed nine successful OCO-3
70 acquisitions of the Bełchatów Power Station and found the variability in satellite-based emission
71 estimates agreed well with the variability in independently reported hourly power generation. Guo et



72 al., (2023) estimated emissions at Chinese power plants using OCO-2/3 and found close agreement
73 with emission inventories. OCO-3 is different than OCO-2 in that it has a two-axis Pointing Mirror
74 Assembly (PMA) for more agile pointing, allowing it to rapidly point off-nadir and take Snapshot
75 Area Mapping (SAM) mode observations over the course of two minutes. These SAMs are
76 approximately 80×80 km² collections of measurements and are typically over sites of interest
77 including cities, power plants, volcanoes, and flux towers.

78 Another class of remote sensing imaging spectrometers – sometimes also referred to as
79 hyperspectral imagers – also have been shown capable of detecting and quantifying strong CO₂
80 signals from large point sources. Thorpe et al. (2017) flew the Next-Generation Airborne/Infrared
81 Imaging Spectrometer (AVIRIS-NG) over a coal-fired power plant in Four Corners, New Mexico,
82 and detected strong CO₂ plumes. AVIRIS-NG observes a large range of solar backscattered radiance
83 (380-2500 nm), but at much coarser spectral resolution (5 nm), and high spatial resolution (e.g., 3 m
84 when flown at 3 km altitude). The much finer spatial resolution of AVIRIS-NG allows for improved
85 visualization of the origin of a CO₂ plume, but at the expense of fine precision for a single observed
86 CO₂ column. Still, Cusworth et al. (2021) analyzed a combination of AVIRIS-NG and the identically
87 built Global Airborne Observatory (GAO) at over 20 power plants in the U.S., quantified emission
88 rates, and found close agreement with continuous emissions monitoring (CEMS) hourly emission
89 observations. The study also showed a few examples of CO₂ plumes detected and quantified with the
90 satellite PRISMA imaging spectrometer (400-2500 nm; 10 nm spectral resolution; 30 m spatial
91 resolution; Loizzo et al., 2018).

92 The capacity for satellites to be leveraged as useful tools for reducing uncertainty in the global
93 CO₂ anthropogenic emission sector requires synthesis and routine tasking of a critical number of
94 facilities. Therefore, in this study, we tasked a subset of global coal-fired power plants routinely over



95 the course of two years to probe detection limits, emission quantification uncertainty, and data yields.
96 We tasked these facilities with both OCO-3 and PRISMA. The results, though not sufficient by
97 themselves to reduce uncertainty relative to bottom-up inventories significantly on an annual basis,
98 show a path forward for data fusion and synthesis of observations from the growing constellation of
99 planned CO₂ sensing satellites.

100

101 **2 Methods**

102 Table 1 lists the locations of all power plants we targeted during this study between 2021-
103 2022 with PRISMA. OCO-3 includes a subset of these sites as well as other fossil fuel combustion
104 sites as part of its list of possible targets. We identified coal-fired power plants to routinely target
105 using a combination of bottom-up and top-down information. Bottom-up coal-fired power plant CO₂
106 emission estimates rely on activity data, that usually includes permitted capacity of a power plant
107 and its operational state; and emission factors, usually estimated from the composition of the coal
108 that is combusted. Inventories, like the Global Energy Monitor (GEM), include this data for a large
109 set of coal-fired power plants across the globe (GEM, 2023). From the GEM database, we gathered
110 the top 10 largest bottom-up coal-fired power plants globally. We then gathered a list of top-down
111 TROPOMI NO₂ combustion hotspots, as inferred by Beirle et al. (2021). We included an additional
112 non-overlapping seven power plants using this dataset. Because the imaging scene size of PRISMA
113 is 30 × 30 km², some adjacent smaller power plants were imaged simultaneously along with these
114 larger power plants. In total, outside of the U.S., we made PRISMA observations at 27 power plants.
115 In the U.S., we chose 10 power plants to routinely target using reported EPA CEMS information
116 (campd.epa.gov): five of the top 30 emitting power plants, and five progressively lower emitters,
117 chosen so that we could assess satellite detection capabilities.



118

119 Table 1. Power plants that were targeted specifically by PRISMA in this study.

Power Plant Name	Country	Latitude	Longitude	Number clear-sky observations	Number plume detections	Minimum quantified CO ₂ emission (kt CO ₂ h ⁻¹)	Mean quantified CO ₂ emission (kt CO ₂ h ⁻¹)	Maximum quantified CO ₂ emission (kt CO ₂ h ⁻¹)
Mundra-Adani	India	22.82	69.55	12	7	0.49±0.07	1.09±0.19	1.76±0.32
Korba-Balco	India	22.40	82.74	5	1	NA*	NA	NA
PLN Paiton Baru	Indonesia	-7.71	113.57	4	2	NA	NA	NA
Craig	USA	40.46	-107.59	5	5	0.56±0.11	0.69±0.16	0.8±0.22
Cumberland	USA	36.39	-87.65	1	0	NA	NA	NA
Dry Fork	USA	44.39	-105.46	6	3	0.61±0.09	0.65±0.13	0.69±0.16
H L Spurlock	USA	38.70	-83.82	5	3	1.15±0.32	1.26±0.39	1.37±0.45
Ulsan Hanju (1)	South Korea	35.49	129.33	1	0	NA	NA	NA
Hasdeo	India	22.41	82.69	5	0	NA	NA	NA
Hekinan	Japan	34.83	136.96	6	4	0.72±0.47	3.88±1.09	8.35±2.14
Baotou-1	China	40.66	109.66	5	2	0.19±0.07	0.27±0.07	0.35±0.07
Kendal	South Africa	-26.09	28.97	7	2	0.85±0.13	0.85±0.13	0.85±0.13
NTPC Korba	India	22.39	82.68	6	1	1.28±0.27	1.28±0.27	1.28±0.27
Kriel	South Africa	-26.25	29.18	8	3	0.74±0.15	0.82±0.15	0.95±0.16
Labadie	USA	38.56	-90.84	4	4	0.73±0.18	0.73±0.18	0.73±0.18
Martin Lake	USA	32.26	-94.57	8	8	1.45±0.31	2±0.59	2.6±0.98
Matimba	South Africa	-23.67	27.61	11	8	0.33±0.05	0.72±0.16	1.14±0.32
Matla	South Africa	-26.28	29.14	8	3	0.33±0.05	0.77±0.15	1.37±0.27
Medupi	South Africa	-23.71	27.56	15	12	0.33±0.06	0.83±0.19	1.47±0.34
Mundra-Tata	India	22.82	69.53	12	5	0.38±0.09	0.74±0.13	1.32±0.21
Niederaussem	Germany	51.00	6.67	1	0	NA	NA	NA
Oregon	USA	41.67	-83.44	5	1	NA	NA	NA
Paiton-3	Indonesia	-7.71	113.58	4	4	1.54±0.37	3.16±0.69	4.78±1.02
Rihand	India	24.03	82.79	8	5	0.83±0.17	0.99±0.26	1.36±0.38
Sanfeng	China	40.66	109.76	6	0	NA	NA	NA
Sasan	India	23.98	82.63	9	7	0.65±0.15	1.01±0.24	1.51±0.31
Sooner	USA	36.45	-97.05	6	3	1.05±0.22	1.05±0.22	1.05±0.22
Togtoh	China	40.20	111.36	2	2	0.25±0.06	0.91±0.17	1.58±0.27



Ulsan Hanju (2)	South Korea	35.47	129.38	1	0	NA	NA	NA
Vindhyachal	India	24.10	82.68	9	7	0.33±0.1	0.72±0.15	1.24±0.23
Waigaoqiao	China	31.36	121.60	6	1	NA	NA	NA
Yeosu Hanwha	South Korea	34.84	127.69	2	0	NA	NA	NA
Yosu	South Korea	34.83	127.67	2	0	NA	NA	NA
Al Zour	Kuwait	28.71	48.37	12	0	NA	NA	NA

120 *A value of “NA” indicates that no plumes were detected at this power plant or that the emission quantification
 121 algorithm (described in Methods) failed to quantify an emission rate.
 122

123 2.2 PRISMA tasking and quantification

124 PRISMA is a tasked satellite instrument, capable of collecting around 200 30 × 30 km² targets
 125 per day and has 20° pointing capability off nadir. Authenticated users can program single task
 126 requests through PRISMA’s web portal (prisma.asi.it), which currently allows for 13 concurrent
 127 requests at a time per user. We specified two-week observing windows for each task request, and
 128 configured tasks to collect if the scene-averaged solar zenith angle (SZA) was less than 70° and
 129 forecast meteorology anticipated less than 20% cloud cover. If the orbital configuration, weather,
 130 SZA align and there are no other conflicting or higher priority task requests, PRISMA images a
 131 target.

132 For each acquired PRISMA image, we performed XCO₂ retrievals on all pixels within a 2.5
 133 km radius around the power plant. We retrieve XCO₂ using the Iterative Maximum A Posteriori –
 134 Differential Optical Absorption Spectroscopy (IMAP-DOAS) algorithm, as implemented in
 135 Cusworth et al. (2021). This approach estimates XCO₂ by decomposing an observed radiance
 136 spectrum into high and low frequency features between 1900-2100 nm. For high-frequency features,
 137 we simulate atmospheric transmission of CO₂, H₂O, and N₂O using a Beer-Lambert approximation.
 138 For low-frequency features (e.g., surface reflectance, aerosol scattering), we use an 8-degree
 139 polynomial. The forward model that drives IMAP-DOAS therefore has the following form:



140
$$F^h(\mathbf{x}) = I_0(\lambda) \exp \left(- \sum_{n=1}^6 s_n \sum_{l=1}^{72} A_l \tau_{n,l} \right) \sum_{k=0}^K a_k \lambda^k \quad (1)$$

141 Where F^h is simulated backscattered radiance at wavelength λ , I_0 is incident solar intensity, A_l is the
142 airmass factor at vertical level $l \in [1,72]$, $\tau_{n,l}$ is the optical depth for each trace gas element, s_n is the
143 scaling factor applied to the optical depth, and a_k is a polynomial coefficient ($K=8$). Optical depths
144 are computed by querying meteorological information for pressure and temperature from the
145 MERRA-2 reanalysis (Gelaro et al., 2017), and using that information to select proper HITRAN
146 absorption cross sections for each trace gas (Kochanov et al., 2016). To compare the model from
147 Equation 1 against PRISMA observed radiance (\mathbf{y}), we compute $F^h(\mathbf{x})$ between 1900-2100 nm at
148 0.02 nm resolution, then convolve the output using the PRISMA full-width half maximum, and
149 sample at PRISMA wavelength positions. This results in vector $\mathbf{F}(\mathbf{x})$ that is comparable to \mathbf{y} . The
150 vector \mathbf{x} , also called the state vector, includes scale factors for CO₂, H₂O, N₂O, and polynomial
151 coefficients: $\mathbf{x} = (s_{CO_2}, s_{H_2O}, s_{N_2O}, a_0, \dots, a_8)$.

152 XCO₂ is retrieved from PRISMA radiance using a Bayesian optimal estimation approach
153 (Rodgers, 2000). Here, the optimized state vector solution, or posterior, is solved through Gauss-
154 Newton iteration:

155
$$\mathbf{x}_{i+1} = \mathbf{x}_A + (\mathbf{K}_i^T \mathbf{S}_0^{-1} \mathbf{K}_i + \mathbf{S}_A^{-1})^{-1} \mathbf{K}_i^T \mathbf{S}_0^{-1} [\mathbf{y} - \mathbf{F}(\mathbf{x}_i) + \mathbf{K}_i(\mathbf{x}_i - \mathbf{x}_A)] \quad (2)$$

156 Where $\mathbf{S}_0 = [\boldsymbol{\epsilon}\boldsymbol{\epsilon}^T]$ is the observation error covariance matrix defined by the instrument signal to noise
157 ratio (SNR), \mathbf{x}_A is the prior estimate of the state vector, and \mathbf{S}_A is the prior error covariance matrix.
158 The matrix \mathbf{K} , or Jacobian matrix, represents the first derivative of the $\mathbf{F}(\mathbf{x})$ with respect to the state
159 vector:

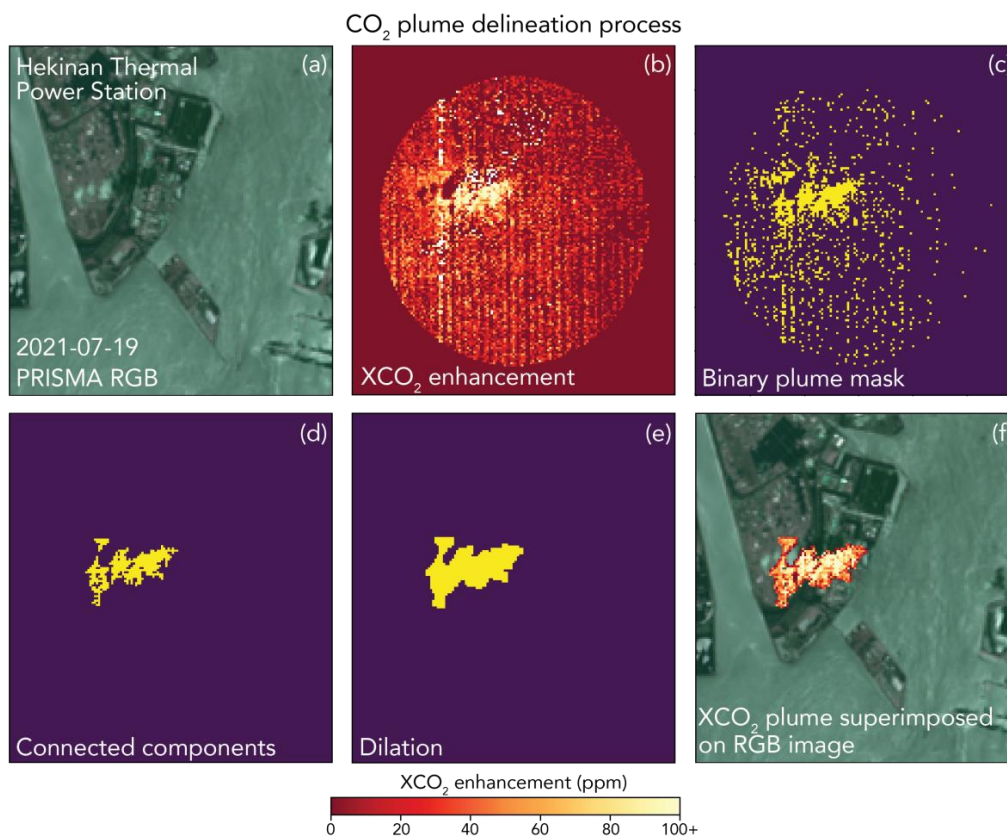
160
$$\mathbf{K}_i = \left. \frac{\partial \mathbf{F}}{\partial \mathbf{x}} \right|_{\mathbf{x}=\mathbf{x}_i} \quad (3)$$



161 The posterior error covariance matrix can be computed explicitly to quantify retrieval precision:

162
$$\hat{\mathbf{S}} = (\mathbf{K}_i^T \mathbf{S}_0^{-1} \mathbf{K}_i + \mathbf{S}_A^{-1})^{-1} \quad (4)$$

163 We quantified each PRISMA plume detection using the Integrated Mass Enhancement (IME)
164 approach (Cusworth et al., 2021). However, we updated the masking scheme for this analysis to
165 produce more reliable masks for each CO₂ plume. Figure 1 shows the plume masking procedure for
166 a plume detected at the Hekinan, Japan power plant on July 19, 2021. First, we apply a background
167 threshold to differentiate candidate plume pixels from the background (method to quantify
168 background threshold described in Results section). We then group enhanced XCO₂ pixels into
169 clusters of at least 20 connected pixels. These groups are then buffered with a one-pixel dilation filter
170 to smooth edges and any gaps that exist in a group. Finally, each cluster is considered part of the
171 plume if at least one of its pixels is within 500 m of an exhaust stack.



172

173 **Figure 1.** Example of the plume delineation and masking process performed on XCO₂ retrievals
 174 derived from PRISMA observations. Panel (a) shows the simultaneously observed RGB PRISMA
 175 imagery, panel (b) shows retrieved XCO₂ above the background, panels (c)-(e) show the plume
 176 masking procedure to isolate enhanced pixels and remove noise, and panel (f) shows the resulting
 177 CO₂ plume superimposed on the RGB imagery.

178

179 IME is calculated for a plume using the following equation:

180

$$\text{IME} = \sum_{i=1}^N \Delta\Omega_i \Lambda_i \quad (5)$$



181 where $\Delta\Omega_i$ is the XCO₂ mass enhancement in pixel i relative to background (kg m^{-2}), Λ_i is the pixel
182 area (900 m^2), and N is the number of pixels in the plume. The CO₂ emission rate Q is estimated from
183 the IME using the following relationship:

$$184 \quad Q = \frac{U_{eff}}{L} \text{IME} \quad (6)$$

185 where $L = \sqrt{\sum_{i=1}^N \Lambda_i}$ is the plume length and U_{eff} is the effective wind speed, which accounts for
186 turbulent dissipation. We estimate U_{eff} from the 10 m wind speed (U_{10}) using a derived empirical
187 relationship (Varon et al., 2018):

$$188 \quad U_{eff} = 1.1 \log U_{10} + 0.6. \quad (7)$$

189 where U_{eff} and U_{10} are in units of [m s^{-1}]. We query the ERA5-Land reanalysis using the Open-Meteo
190 Application Programming Interface (open-meteo.com), which provides hourly wind information
191 globally at 0.1° spatial resolution (Muñoz-Sabater et al., 2021). Uncertainty due to winds is calculated
192 by generating an ensemble of U_{10} values assuming 50% error (Cusworth et al., 2021). Uncertainty
193 due to the CO₂ background is calculated by generating many emission estimates and calculating a
194 standard deviation using an ensemble of background thresholds. Background thresholds are set to
195 vary with scene-averaged CO₂ retrieval precision. Total emission uncertainty is estimated by adding
196 in quadrature the contribution of wind and background uncertainties.

197

198 *2.3 OCO-3 tasking and quantification*

199 OCO-3 is also a tasked mission: it can take SAMs over any place of interest within the latitude
200 range of the ISS orbit (about 52° S to 52° N). In addition to the SAM locations we supplied to OCO-
201 3 to overlap with PRISMA targets, there are many other power plant and fossil fuel combustion
202 sources that make up its set of mission targets. However, unlike PRISMA, OCO-3 does not consider



203 cloud forecasts, snow cover, or viewing geometry when planning SAMs and thus the majority of
204 observations fail to produce useful maps of XCO₂. Additionally, aerosol- and albedo-induced XCO₂
205 artifacts are present in many SAMs (Bell et al., 2023) and thus make the detection of plumes even
206 more difficult.

207 For all cloud-free soundings, OCO-3 XCO₂ concentrations are derived using the
208 Atmospheric Carbon Observations from Space (ACOS; O'Dell et al., 2012; Crisp et al., 2012; O'Dell
209 et al., 2018) v10 optimal estimation retrieval, which employs the Levenberg-Marquardt modification
210 of the Gauss-Newton method. In this work, bias corrected XCO₂ from the OCO-3 Lite files is used
211 but the official data quality flag is not applied. This was done because often the quality flag removes
212 XCO₂ retrievals within the plume and makes emission estimation more difficult or impossible
213 (Nassar et al., 2022). For SAMs where we visually identified CO₂ plumes (e.g., Figure 2), emission
214 rates are estimated using two approaches: (1) a Gaussian plume model and (2) the IME method. For
215 the Gaussian plume model approach, we follow the algorithm outlined in Nassar et al. (2022):

$$216 \quad V(x, y) = \frac{Q}{\sqrt{2\pi}\sigma_y(x)u} e^{-\frac{1}{2}\left(\frac{y}{\sigma_y(x)}\right)^2} \quad (8)$$

$$217 \quad \sigma_y(x) = a \cdot \left(\frac{x}{x_o}\right)^{0.894} \quad (9)$$

218 Where V represents the vertical columns within the plume (g/m²), Q is the CO₂ emission rate (g/s),
219 y is the wind direction perpendicular to the plume (m), u is the wind speed at the height of the plume
220 at its midline (m/s) assuming plume rise of 250 m above the stack height, $\sigma_y(x)$ is the standard
221 deviation of the y -direction, x_o is a characteristic plume length (1000 m), and a is a stability
222 parameter (Nassar et al., 2021). Following Nassar et al. (2022), wind speed and direction inputs are
223 estimated by taking the average of ERA-5 (Bell et al., 2020) and MERRA-2 reanalysis data. The
224 wind direction is optimized by rotating the plume, typically between -30° to 30° away from the mean



225 ERA-5/MERRA-2 direction, and calculating the correlation coefficient (R) of the modeled and
226 observed XCO_2 . The optimized wind direction is the direction that produces the largest R . The
227 background is typically estimated by averaging OCO-3 footprints within a radius of 30 km, excluding
228 the plume itself and a narrow 3 km buffer zone. However, if there are visible artifacts in the XCO_2
229 background that are unrelated to the power plant plume, the background field is modified to avoid
230 them. For example, decreasing the radius of footprints used from 30 km to 20 km. The uncertainty
231 in wind speed is calculated by taking the difference of the emission estimate using two different
232 models (ERA-5 and MERRA2). The background concentration uncertainty is calculated by
233 estimating Q using three different background radii of 30, 40, and 50 km. Q is also calculated for a
234 30 km radius background but only using the left and right halves of the background, relative to the
235 direction of the plume. The standard deviation of both these methods is calculated and the larger of
236 the two is the background uncertainty. The plume rise uncertainty is calculated by estimating Q using
237 plume rise values of 100, 200, 250, 300, and 400 m and taking the standard deviation of those values.
238 Total uncertainty on the emission rate Q using the Gaussian plume method is estimated by adding in
239 quadrature the contribution of wind speed, background concentration, and plume rise uncertainties.

240 To obtain another estimate of emission rate, we also apply an IME quantification approach to
241 the CO_2 plumes, which to our knowledge is the first time the IME method has been applied to OCO-
242 3 SAMS at coal power plants. We first interpolate the XCO_2 retrievals in a SAM to a uniform 2×2
243 km^2 grid to account for occasional OCO-3 footprint overlap. Similar to Varon et al. (2018), 3×3
244 pixel neighborhoods are sampled and the distributions are compared to the background using a
245 Student's t -test. The default confidence level for the t test is 95% but this is often lowered to visually
246 capture most of the plume. The plume is then smoothed using a 3×3 pixel median filter and a
247 Gaussian filter with a standard deviation of 0.5. The U_{eff} calculation is done using an equation

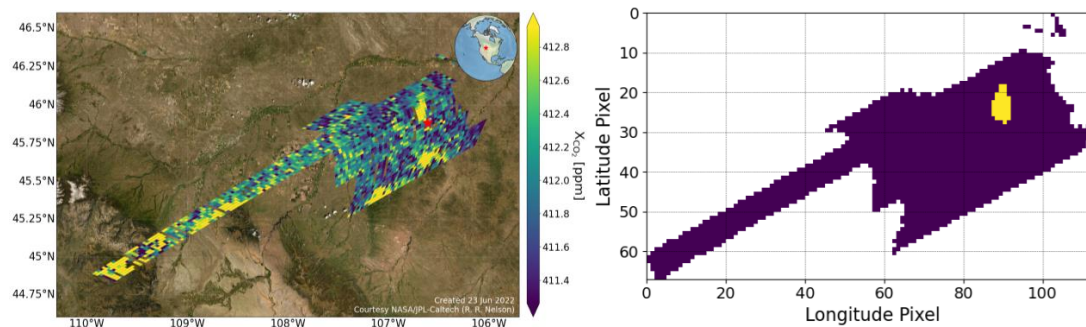


248 approximately equal to Equation 7 ($U_{eff} = 1.0 \log U_{10} + 0.55$). Other recent studies have used various
249 methods (Lin et al., 2023; Brunner et al., 2023), but further research is needed to determine the most
250 accurate way to estimate U_{eff} for an OCO-3-like instrument. The wind direction is the optimized
251 direction determined by the Gaussian plume model. The background XCO₂ estimate is taken from
252 the Gaussian plume model methodology and the plume is typically required to be within 50 km
253 downwind and 8 km crosswind of the source, although these parameters are modified if the plume
254 curves outside of the 8 km crosswind threshold or there are XCO₂ artifacts that should be avoided.

255 The uncertainty for the IME method is estimated similarly to the Gaussian plume model
256 method. The uncertainty in wind speed is calculated by taking the standard deviation of the emission
257 estimates using wind speed from two different models (ERA-5 and MERRA2). The background
258 concentration uncertainty is calculated by estimating Q using the different backgrounds calculated in
259 the Gaussian plume model method: a 20 km radius, 30 km radius, 40 km radius, left half, full circle,
260 and right half. The standard deviation of the three radii estimates and left half, full circle, and right
261 half estimates are calculated and the larger of the two is the background uncertainty. Uncertainty of
262 the Student's t -test confidence level is also estimated. The confidence level and -10% and +10% of
263 the confidence level are used to find Q . For example, if the confidence level needed to visually
264 capture the XCO₂ plume is 85%, Q is calculated for 75%, 85%, and 95% and the standard deviation
265 of those three values represents the confidence level uncertainty. Total uncertainty on the emission
266 rate Q using the IME method is estimated by adding in quadrature the contribution of wind speed,
267 background concentration, and Student's t -test confidence level uncertainties.

268 Figure 2 shows IME methodology successfully identifying an XCO₂ plume from an OCO-3
269 SAM taken over the Colstrip power plant.

270



271

272 **Figure 2.** IME plume identification approach applied to an example OCO-3 SAM at the Colstrip
273 power plant on 18 August 2021. Left panel: OCO-3 SAM bias corrected XCO₂. Right panel: yellow
274 pixels indicate the final plume mask.

275

276 **3 Results**

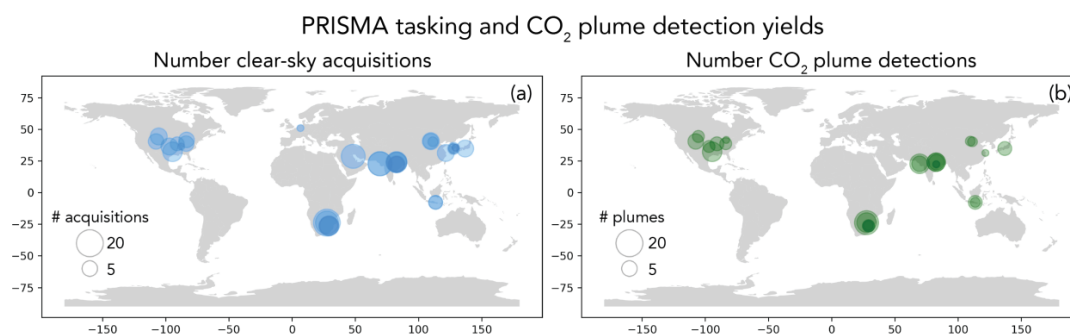
277 *3.1 Global yields from two years of tasking*

278 Figure 3a shows a global map of power plants we targeted with PRISMA, with the marker
279 for each power plant's location (latitude, longitude) scaled to represent the number of successful
280 acquisitions between 2021-2022. In total, we acquired 181 PRISMA images, which corresponds to
281 314 unique power plant observation scenes. Of these scenes, 210 were of sufficient quality to attempt
282 CO₂ retrieval and plume detection, with quality mostly determined by visual inspection for clouds
283 and haze. Of these 210 scenes, 104 were determined to have CO₂ plumes (Figure 3b). Scenes were
284 marked as containing CO₂ plumes through inspection of XCO₂ and visible imagery: if a large cluster
285 of pixels with elevated XCO₂ above the background were also in the vicinity of a power plant exhaust
286 stack, an analyst would mark the scene as containing a CO₂ plume. Tasking with PRISMA resulted
287 in an average of 6 acquisitions for each power plant (maximum 15), roughly one image acquired per



288 quarter. Of these acquisitions, plumes were detected on average four times per facility (maximum
289 12).

290 For OCO-3, 1363 power plant SAMs were taken during September 2019 to December 2022.
291 Of these, 139 XCO₂ plumes emanating from power plants were visually identified. However, only
292 14 were for power plants that were also tasked by PRISMA and have CEMS validation (nine Colstrip
293 cases, two Martin Lake cases, and three Craig cases). The acquisition rates are low relative to
294 PRISMA because OCO-3 does not account for scene favorability when planning its SAMs. For
295 example, OCO-3 took 66 Colstrip SAMs from 2019-2022 yet only yielded nine high-quality XCO₂
296 plume cases.



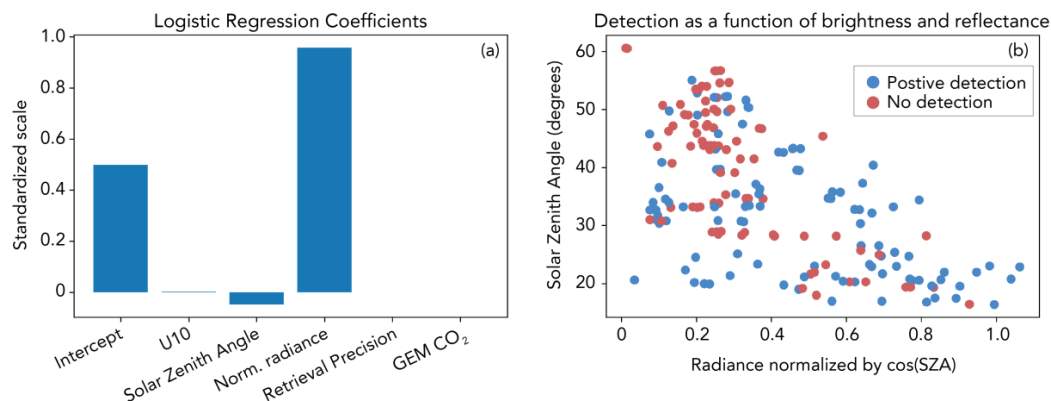
297 **Figure 3.** Data yields from tasking PRISMA continually between 2021-2022. Panel (a) shows the
298 number of clear-sky acquisitions for each power plant. Panel (b) shows the number of plumes
299 detected by an analyst for each of the tasked power plants.
300

301
302 The low observed average detection rate of plumes for PRISMA (50%) is a result of three
303 primary factors: (1) observing conditions at each facility including solar zenith angle (SZA) and
304 surface reflectance; (2) local meteorology; and (3) operational status at each power plant at the time
305 of acquisition. To test how well these factors predict the presence of a plume, we fit a logistic



306 regression classification function with a sparse (L1) penalty to our dataset (Fan et al., 2008). In this
307 setup, the statistical model is fit using the following predictor variables – SZA, U_{10} , average single-
308 sounding retrieval precision across the scene, annual bottom-up emission estimate for the power plant
309 using GEM, and average observed radiance between 1900-2100 nm within the scene normalized by
310 the cosine of the SZA. This last factor is a simple proxy for surface reflectance, although it does not
311 take into account other factors that influence radiance observations (e.g., water vapor, aerosols, other
312 atmospheric constituents). We split the data so that 50% was used to train the model and 50% was
313 reserved as a test set. The predictor variables were all standardized by their mean and standard
314 deviation before the model was fit. The results of classification can be summarized using two
315 statistics: precision (ratio of true positives to sum of true positives and false positives) and recall
316 (ratio of true positives to sum of true positives and false negatives). The results of fitting a logistic
317 regression model to the data show minor prediction performance, with precision = 0.60 and recall =
318 0.69 for positive plume detection. The regression coefficients are shown in Figure 4a. The coefficient
319 with the highest weight is normalized radiance. Figure 4b shows SZA against normalized radiance,
320 with red dots indicating no plume detection and blue dots representing positive plume detection.
321 Though no clear separation exists, there is a cluster of no plume detection at high SZA and low
322 normalized radiance. This is a consistent and expected relationship, as SZA and surface reflectance
323 are principal drivers of the quantity of light that is observed by the satellite, and therefore SNR of the
324 observation.

325



326

327 **Figure 4.** CO₂ plume prediction using various atmospheric, retrieval, and bottom-up information.

328 Panel (a) shows the results of fitting a logistic regression classification model to the set of PRISMA

329 acquisitions where an analyst identified the presence or lack of a plume. Panel (b) shows the top two

330 explanatory variables (SZA and normalized radiance) along with plume classification.

331

332 The logistic regression model performed better on the test data set than predictions made at

333 random, though the prediction performance was still low. Missing from the model is sub-annually

334 resolved information regarding operating status. For most of the power plants outside the U.S., we

335 do not have information on daily operations of a power plant. In many cases of non-detects, we could

336 simply be observing a power plant temporarily not in operation. Another possibility is that at the time

337 of acquisition, some power plants were operating at reduced capacity, meaning that CO₂ emission

338 rates were lower than those predicted by annual emission factors or activity data. If the true CO₂

339 emission rate was below the minimum detection limit (MDL) possible by the PRISMA satellite, then

340 it would show as a non-detect. However, even if the emission were near or slightly above the

341 PRISMA MDL, the probability of detection would still be low as slight variations in atmospheric

342 properties, as seen in Figure 4, would then influence the ability to detection a CO₂ plume.



343

344 *3.2 Validation of PRISMA and OCO-3 emission rates against CEMS*

345 For each power plant where a CO₂ plume was identified, we quantify emissions using the
346 IME approach described by Equations 5-7. In order to estimate the XCO₂ mass enhancement ($\Delta\Omega$ in
347 Equation 1), a local background must be quantified and subtracted from total XCO₂ retrievals across
348 the scene. To do this, we apply a concentration threshold β to initiate the plume masking and
349 segmentation process (described in Methods section). Once we have a plume mask, we apply another
350 concentration threshold γ to the remaining XCO₂ pixels that exist outside of the plume. This value γ
351 represents the XCO₂ background that we use to calculate the XCO₂ enhancement that is used in the
352 IME formulation of Equation 1. Thresholds β and γ largely influence the magnitude of the emission
353 rate and are not known a priori. For global generalizability, we wish to estimate β and γ such that
354 they do not vary across power plants, seasons, regions, etc. Therefore, we parameterize β and γ as
355 percentiles under the assumption that the local contrast between enhanced CO₂ plume pixels and the
356 background should be similar across PRISMA scenes.

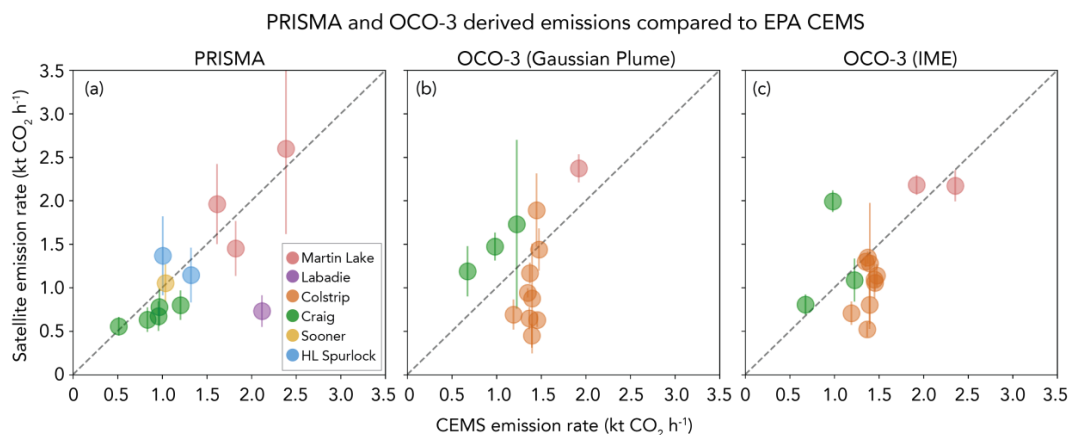
357 To estimate values for β and γ , we compare EPA CEMS data for power plants in the U.S.
358 with estimated emission rates from PRISMA. In total, we have 12 scenes in the U.S. with CEMS
359 information that pertain to 5 power plants. We then optimize β and γ such that the output of an
360 ordinary least squares regression produces a slope near unity. Figure 5a shows the results of this
361 optimization which produces an optimal β percentile of 94% and a γ percentile of 62%. The results
362 also show decent correlation between CEMS data and PRISMA-derived emission rates ($R^2 = 0.43$).
363 A single outlier at the Labadie power plant (imaged July 10, 2022) shows the largest discrepancy
364 from CEMS data (69%), but the remaining plumes show average 27% relative difference from CEMS
365 data. If we remove the one data point at Labadie, the R^2 improves to 0.75. Though a limited sample



366 size, between PRISMA and OCO-3, these scenes represent variability in solar geometries (20-40°
367 SZA), surface reflectance (0.09-0.90 normalized radiance), and reported emission rates (0.51 – 2.39
368 kt CO₂ h⁻¹). Therefore, we use these optimal parameters and apply them to our global dataset of
369 PRISMA detections. These emission rates are reported in Table 1. There are some instances when
370 performing IME emission calculations using these thresholds and plume masking technique do not
371 result in emission rates (e.g., the plume masking procedure produces a mask with no pixels). In these
372 cases, we report a detection but not an emission quantification.

373 Figures 5b and 5c shows the comparison between OCO-3 and CEMS at some power plants
374 that overlap with PRISMA tasking (14 scenes total). OCO-3 Gaussian plume model emission rates
375 (Fig. 5b) have an improved correlation compared to PRISMA ($R^2 = 0.51$), although with greater bias
376 (average 47% relative difference from CEMS). The OCO-3 IME estimates (Fig. 5c) have worse R^2
377 (0.32) but a better RMSE (0.45 kt CO₂/hr) compared to the Gaussian plume model estimates (0.84 kt
378 CO₂/hr), with 9 of the 14 cases being within 30% of the reported CEMS emission and an average
379 relative difference of 30% for all 14 cases. Additionally, the least squares fit for IME is closer to the
380 1-to-1 line than for the Gaussian plume model.

381



382

383 **Figure 5.** Comparison of emission rates in the U.S. between satellite-derived estimates and CEMS
 384 information. Panel (a) shows a comparison between PRISMA derived emission rates and CEMS (R^2
 385 = 0.43), panel (b) shows a comparison between OCO-3 and CEMS using the Gaussian plume model
 386 ($R^2 = 0.51$), and panel (c) shows a comparison between OCO-3 and CEMS using IME ($R^2 = 0.32$).

387

388 Unique sources of error for OCO-3 emission estimates include geolocation errors in the
 389 XCO₂ product. These errors are typically less than 1 km, but can be up to 2 km (Taylor et al., 2023).
 390 Errors of this magnitude, about the size of an OCO-3 footprint ($\sim 2 \times 2$ km²), may mean that an entire
 391 footprint is not included when estimating emissions using the Gaussian plume method, which
 392 assumes that the plume only extends downwind of the known source location. The Gaussian plume
 393 model is also susceptible to wind direction errors, and requires the plume to be Gaussian in shape,
 394 which is often not true. IME, while not suffering from wind direction or geolocation-induced errors,
 395 assumes that the entire plume is captured in a given SAM, which is sometimes not true and results in
 396 an underestimation of emissions. IME is also sensitive to errors in U_{eff} parameterization.

397



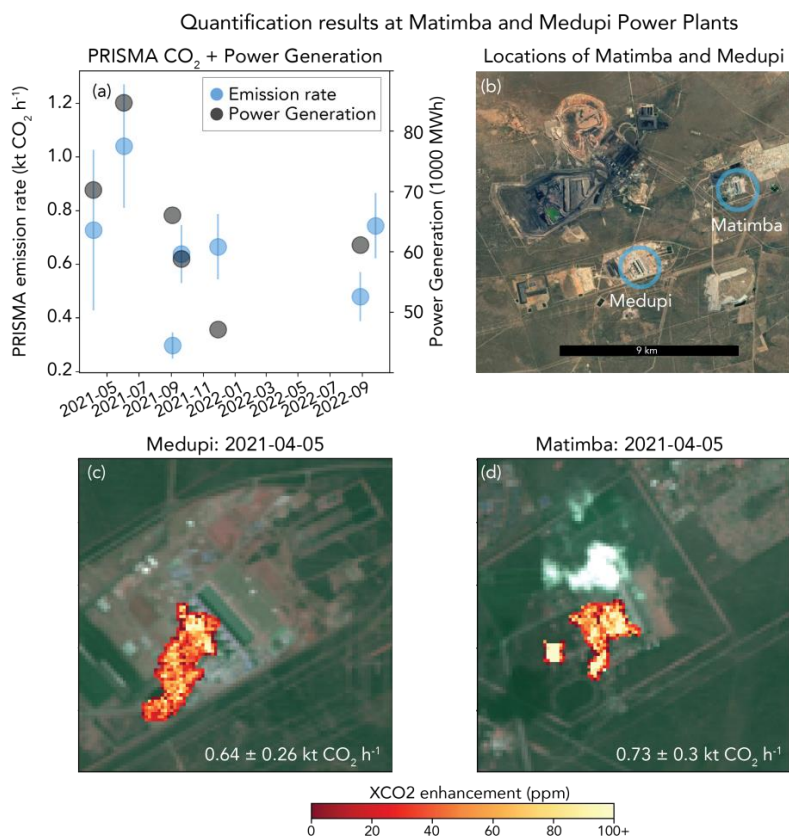
398 *3.3 Comparison and fusion of PRISMA and OCO*

399 Outside the U.S., PRISMA observed the Matimba power station in South Africa 11 times and
400 quantified emission rates 7 times. Emissions from Matimba have previously been quantified and
401 validated using OCO-2 (Hakkarainen et al., 2021). This station does not report hourly emission rates,
402 but does report daily power generation (Eskom, 2023). Though not a direct comparison, we can use
403 this information to check if the emission quantification approach we describe above captures some
404 variability in activity at this power plant. Figure 6a shows the emission rates we quantified compared
405 against reported power generation. We see rough agreement in variability – the high power
406 generation reported between Apr to July 2021 (70000-85000 MWh) drop for subsequent dates
407 (47000-66000 MWh) between Sep 2021 to Sep 2022, a drop which is also seen in the PRISMA-
408 derived CO₂ emission rate. Across all observations, we estimate an emission rate range of 0.30-1.04
409 kt CO₂ h⁻¹ (average 0.66 kt CO₂ h⁻¹). This average emission rate is substantially lower than the
410 average 2.50 kt CO₂ h⁻¹ emission rate estimated from OCO-2 and TROPOMI between 2018-2020,
411 but within the range of emissions estimates directly quantified with OCO-2 (0.30-7.20 kt CO₂ h⁻¹;
412 Hakkarainen et al., 2021). However, this discrepancy could be result of (1) changes in activity or
413 variability or (2) existence of other nearby emission sources. For changes in activity, during August
414 2020, the Matimba reported a large range of power generation (65000-94000 MWh) and emission
415 estimates derived directly from OCO-2 were also highly variable (0.88-4.33 kt CO₂ h⁻¹). Given that
416 maximum power generation at the time of a PRISMA observation was 85000 MWh, some of the
417 discrepancy in maximum CO₂ quantification between PRISMA and OCO-2 could be due to activity.

418 Nearby (7 km) the Matimba Power Station is the Medupi Power Plant (Figure 6b). Figure 6c
419 show the Medupi CO₂ plume observed during the same PRISMA overpass on Apr 5, 2021. The
420 PRISMA derived emission rate for Medupi is 0.64 ± 0.26 kt CO₂ h⁻¹ and for Matimba is 0.73 ± 0.30



421 kt CO₂ h⁻¹. Given the proximity of the two power plants, the higher derived emission rate reported
 422 for Matimba from previous studies could actually be a result of a net emission from these two
 423 facilities. The OCO-2 flight track is located tens of kilometers downwind from Matimba and Medupi,
 424 making a clear delineation between potentially co-emitted distinct emission plumes near impossible.
 425 If we sum emission rates from both Medupi and Matimba, we quantify a range of 0.89-1.73 kt CO₂
 426 h⁻¹ (1.30 ± 0.28 kt CO₂ h⁻¹), which is still lower, but closer to the average emissions quantified by
 427 OCO-2.



428

429 **Figure 6.** Emission rates and reported power generation at the Matimba and Medupi power plants in
 430 South Africa. Panel (a) shows the CO₂ emission rates derived from PRISMA and the reported daily



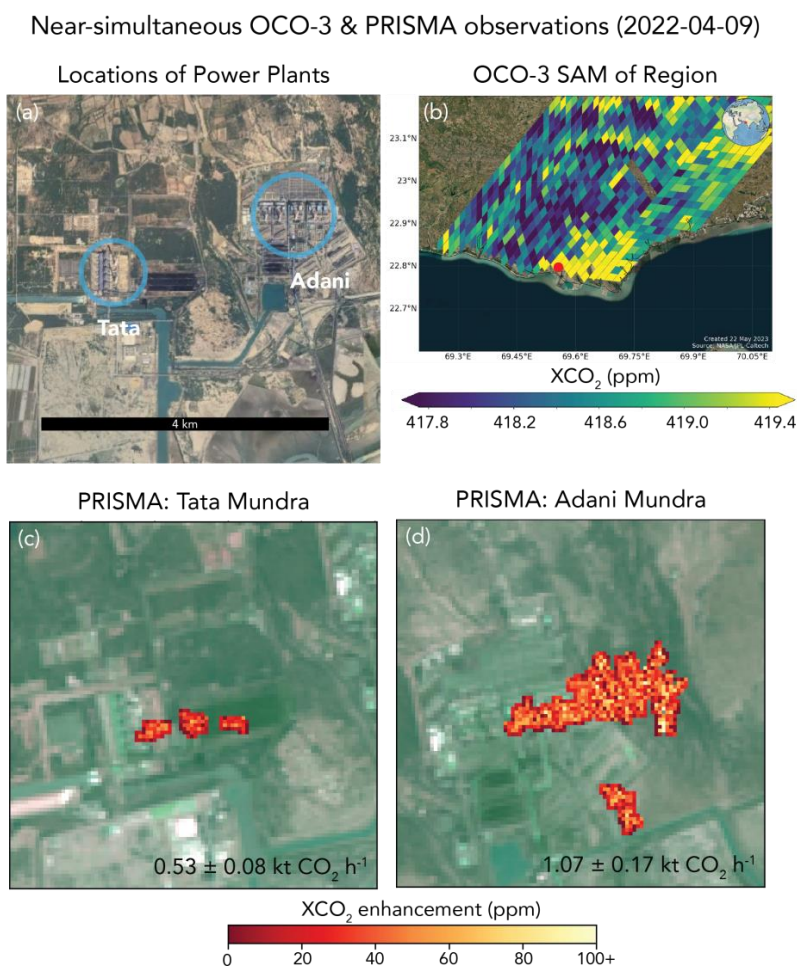
431 power generation for the day of PRISMA overpass. Panel (b) shows the locations of the Medupi and
432 Matimba power plants (base imagery provided by Google Earth; © Google Earth 2023). Panels (c)
433 and (d) show plume imagery and emission rates for a PRISMA overpass on Apr 5, 2021.

434

435 The ability to differentiate the contribution of unique point sources to a regional total is an
436 application made possible by joint observing of imaging spectrometers and atmospheric sounders.
437 Figure 7 shows observations that were made at the Tata Mundra Ultra Mega Power Plant and the
438 Adani Mundra Thermal Power Project: two power plants less than 3 km apart. Both OCO-3 and
439 PRISMA imaged the power plants on Apr 9, 2022. Figure 7b shows the OCO-3 SAM (taken 04:41
440 UTC) – large CO₂ enhancements appear along the coastline likely associated with emission from
441 these power plants. PRISMA imaged the power plants less than two hours later (06:02 UTC) and
442 detected CO₂ plumes at each facility (Figure 7b-c). The OCO-3 derived emission rate using Gaussian
443 plume approaches is 5.5 ± 0.7 kt CO₂ h⁻¹, but the emission rate derived using the IME approach is
444 much lower (3.0 kt CO₂ h⁻¹). For this case, the IME approach may be more appropriate as the shape
445 of the OCO-3 plume (Figure 7b) is more diffuse in nature and does not visibly resemble a Gaussian
446 structure. The PRISMA emission rate for the Adani plant is 1.07 ± 0.17 kt CO₂ h⁻¹ and for the Adani
447 plant is 0.53 ± 0.08 kt CO₂ h⁻¹. We can use this information to estimate that 67% of the net CO₂
448 emission came from Adani, and the remaining 33% came from the Tata plant. The combined
449 emission rate (1.60 ± 0.25 kt CO₂ h⁻¹) is lower than the OCO-3 IME emission rate. Like the Matimba
450 power plant, some of this discrepancy is likely explained by uncertainty in retrievals, background,
451 and wind information. Continued validation of retrieved emission rates against ground standards
452 (e.g., CEMS) will help reduce this uncertainty. However, even with this lingering uncertainty, the



453 near simultaneous observations of OCO-3 and PRISMA can help us disentangle the relative
454 contributions from each power plant.
455



456
457 **Figure 7.** Near-simultaneous observation of two power plants in Mundra, India on Apr 9, 2022. Panel
458 (a) shows the locations of two power plants spaced less than 3 km apart: Tata Mundra and Adani
459 Mundra Power Stations (base imagery provided by Google Earth; © Google Earth 2023). Panel (b)
460 shows the OCO-3 SAM with a red dot showing the location of the power plants. Panel (c) and (d)



461 show the PRISMA acquisition (less than 2 hours after OCO-3) over the two power plants with
462 associated emission rates.

463

464 **Conclusion**

465 We tasked a global set of power plants for two years between 2021-2022 with both PRISMA
466 and OCO-3 to test the ability of these satellite platforms to do routine operational monitoring of CO₂
467 emissions. When PRISMA observations were of sufficient quality to perform XCO₂ retrievals, we
468 detected CO₂ plumes nearly half of the time. We fit a logistic regression classification using plume
469 detections and find that there is some relationship between SZA and surface reflectance that partially
470 explains plume prediction; consistent given that these factors are major drivers of SNR. The
471 remaining non-plume detections may be due to operational status of a power plant at the time of
472 observation. We compared emission rates from both PRISMA and OCO-3 to power plants in the
473 U.S. where we have access to hourly *in situ* CEMS emission information. We find significant
474 correlation between satellite and *in situ* estimates, though some significant biases may exist for some
475 of the observations for both PRISMA and OCO-3. Also, the quantity of CEMS observations was
476 limited (~10 for each instrument), so robust calibration is not yet possible. Still, early results show
477 that under the right conditions, satellites can provide reliable estimates of CO₂ emissions at discrete
478 point source locations. This is consistent with the close agreement between airborne imaging
479 spectrometer emissions and CEMS information (Cusworth et al., 2021).

480 Fusion of information from atmospheric sounders like OCO-3 and imaging spectrometers
481 like PRISMA is valuable for cross-validation and source attribution. We see this particularly for our
482 examples at the Matimba and Medupi power plants in South Africa and the Tata and Adani power
483 plants in Mundra, India. In these cases, and particularly at Mundra where near-simultaneous



484 PRISMA and OCO-3 observations were taken, OCO-2/3 provides a local, but coarse resolution
485 emission constraint for a complex of facilities that emit large CO₂ quantities. PRISMA, with its 30
486 m pixel resolution, then can help refine relative contributions of single emitters against the net
487 emission flux. More work is needed to refine cross-validation between instruments, but initial tasking
488 shows one avenue for data from multiple observing systems to be complementary aggregated and
489 analyzed.

490 Even when combining information from both satellites, there is still too little sampling to
491 constrain facility emissions within low uncertainties. Cusworth et al. (2021), using arguments from
492 Hill and Nassar (2019), suggested that nearly 30 unbiased observations from a PRISMA-class
493 instrument is needed per year at each power plant to reduce annual uncertainties below 14% (i.e.,
494 reduce emission uncertainty from Non-Annex I countries below 1 Gt CO₂ per year). No power plant
495 in this study met this minimum sampling requirement. However, there will be a significant increase
496 in data volumes and observation performance of satellite remote sensing capabilities for CO₂, from
497 both recently launched and planned imaging spectrometers including EMIT (launched 2022; Thorpe
498 et al., in revision); EnMAP (launched 2022; Guanter et al., 2015); Carbon Mapper/Tanager 1-2
499 (Planned launch 2024; Duren et al., 2021), and atmospheric sounders including CO₂M (Sierk et al.,
500 2019). Improved observation of global power plants and emission quantification with robust error
501 characterization will be vital to reduce global uncertainty of anthropogenic emissions from fossil fuel
502 combustion sources.

503

504 **Data Availability.**

505 The OCO-3 XCO₂ and other retrieval properties are publicly available at the NASA Goddard Earth
506 Science Data and Information Services Center (GES-DISC). The full suite of retrieval products in



507 the standard per-orbit format can be obtained at OCO Science Team et al., 2021,
508 <https://doi.org/10.5067/D9S8ZOCHCADE>. The lightweight per-day format data (Lite files), which
509 includes the bias corrected estimates of XCO₂, can be obtained at OCO Science Team et al., 2022,
510 <https://doi.org/10.5067/970BCC4DHH24>. PRISMA data including radiance for each scene and
511 XCO₂ retrievals is available at <https://doi.org/10.5281/zenodo.8083596>.

512

513 **Acknowledgments.** This work was supported by the Orbiting Carbon Observatory Science Team.
514 We thank the Italian Space Agency for the PRISMA satellite targets. Portions of this work were
515 undertaken at the Jet Propulsion Laboratory, California Institute of Technology, under contract with
516 NASA.

517

518 **Author Contributions.** DHC designed the study. DHC, AKA, RJ tasked and acquired PRISMA
519 data. DHC performed PRISMA emission quantification and validation. RRN performed OCO-3
520 quantification and validation. RN and JPM helped implement OCO-3 quantification algorithms. All
521 authors provided feedback on results and the manuscript.

522

523

524 **Competing interests.** The authors declare no conflicts of interest.

525

526 **References**

527 Beirle, S., Borger, C., Dörner, S., Eskes, H., Kumar, V., de Laat, A. and Wagner, T., 2021. Catalog
528 of NO_x emissions from point sources as derived from the divergence of the NO₂ flux for
529 TROPOMI. *Earth System Science Data*, 13(6), pp.2995-3012.



530

531 Bell, B., Hersbach, H., Berrisford, P., Dahlgren, P., Horányi, A., Sabater, M., et al.
532 (2020). ERA5 hourly data on pressure levels from 1950 to 1978 (preliminary
533 version). Copernic. Clim. Change Serv. (C3S) Clim. Data Store (CDS). Available at:
534 [https://cds.climate.copernicus-climate.eu/cdsapp#!/dataset/reanalysis-era5-](https://cds.climate.copernicus-climate.eu/cdsapp#!/dataset/reanalysis-era5-pressure-levels-preliminary-back-extension?tab=overview)
535 [pressure-levels-preliminary-back-extension?tab=overview](https://cds.climate.copernicus-climate.eu/cdsapp#!/dataset/reanalysis-era5-pressure-levels-preliminary-back-extension?tab=overview).

536

537 Bell, E., O'Dell, C.W., Taylor, T.E., Merrelli, A., Nelson, R.R., Kiel, M., Eldering, A., Rosenberg,
538 R. and Fisher, B., 2023. Exploring bias in the OCO-3 snapshot area mapping mode via geometry,
539 surface, and aerosol effects. *Atmospheric Measurement Techniques*, 16(1), pp.109-133.

540

541 Brunner, D., Kuhlmann, G., Henne, S., Koene, E., Kern, B., Wolff, S., Voigt, C., Jöckel, P.,
542 Kiemle, C., Roiger, A. and Fiehn, A., 2023. Evaluation of simulated CO₂ power plant plumes
543 from six high-resolution atmospheric transport models. *Atmospheric Chemistry and Physics*, 23(4),
544 pp.2699-2728.

545

546 Crippa, M., Oreggioni, G., Guizzardi, D., Muntean, M., Schaaf, E., Lo Vullo, E., Solazzo, E.,
547 Monforti-Ferrario, F., Olivier, J.G. and Vignati, E., 2019. Fossil CO₂ and GHG emissions of all
548 world countries. *Publication Office of the European Union: Luxembourg*.

549

550 Crisp, D., Fisher, B.M., O'Dell, C., Frankenberg, C., Basilio, R., Bösch, H., Brown, L.R., Castano,
551 R., Connor, B., Deutscher, N.M. and Eldering, A., 2012. The ACOS CO₂ retrieval algorithm—part
552 II: global X CO₂ data characterization. *Atmospheric Measurement Techniques*, 5(4), pp.687-707.



553

554 Cusworth, D.H., Duren, R.M., Thorpe, A.K., Eastwood, M.L., Green, R.O., Dennison, P.E.,
555 Frankenberg, C., Heckler, J.W., Asner, G.P. and Miller, C.E., 2021. Quantifying global power plant
556 carbon dioxide emissions with imaging spectroscopy. *AGU Advances*, 2(2), p.e2020AV000350.

557

558 Duren, R., Cusworth, D., Ayasse, A., Herner, J., Thorpe, A., Falk, M., Heckler, J., Guido, J.,
559 Giuliano, P., Chapman, J. and Green, R., 2021, December. Carbon Mapper: on-orbit performance
560 predictions and airborne prototyping. In *AGU Fall Meeting Abstracts* (Vol. 2021, pp. A53F-05).

561

562 Eldering, A., Taylor, T.E., O'Dell, C.W. and Pavlick, R., 2019. The OCO-3 mission: measurement
563 objectives and expected performance based on 1 year of simulated data. *Atmospheric Measurement*
564 *Techniques*, 12(4), pp.2341-2370.

565

566 Fan, R.E., Chang, K.W., Hsieh, C.J., Wang, X.R. and Lin, C.J., 2008. LIBLINEAR: A library for
567 large linear classification. *the Journal of machine Learning research*, 9, pp.1871-1874.

568

569 Gelaro, R., McCarty, W., Suárez, M.J., Todling, R., Molod, A., Takacs, L., Randles, C.A.,
570 Darmenov, A., Bosilovich, M.G., Reichle, R. and Wargan, K., 2017. The modern-era retrospective
571 analysis for research and applications, version 2 (MERRA-2). *Journal of climate*, 30(14), pp.5419-
572 5454.

573



574 GEM, Global Energy Monitor's Global Coal Plant Tracker, URL
575 <https://globalenergymonitor.org/projects/global-coal-plant-tracker/tracker/>, last accessed May 24,
576 2023
577
578 Guan, D., Liu, Z., Geng, Y., Lindner, S. and Hubacek, K., 2012. The gigatonne gap in China's
579 carbon dioxide inventories. *Nature Climate Change*, 2(9), pp.672-675.
580
581 Guanter, L., Kaufmann, H., Segl, K., Foerster, S., Rogass, C., Chabrillat, S., Kuester, T., Hollstein,
582 A., Rossner, G., Chlebek, C. and Straif, C., 2015. The EnMAP spaceborne imaging spectroscopy
583 mission for earth observation. *Remote Sensing*, 7(7), pp.8830-8857.
584
585 Guo, W., Shi, Y., Liu, Y. and Su, M., 2023. CO₂ emissions retrieval from coal-fired power plants
586 based on OCO-2/3 satellite observations and a Gaussian plume model. *Journal of Cleaner*
587 *Production*, 397, p.136525.
588
589 Hakkarainen, J., Szeląg, M.E., Ialongo, I., Retscher, C., Oda, T. and Crisp, D., 2021. Analyzing
590 nitrogen oxides to carbon dioxide emission ratios from space: A case study of Matimba Power
591 Station in South Africa. *Atmospheric Environment: X*, 10, p.100110.
592
593 Hill, T. and Nassar, R., 2019. Pixel size and revisit rate requirements for monitoring power plant
594 CO₂ emissions from space. *Remote Sensing*, 11(13), p.1608.
595



596 Hong, C., Zhang, Q., He, K., Guan, D., Li, M., Liu, F. and Zheng, B., 2017. Variations of China's
597 emission estimates: response to uncertainties in energy statistics. *Atmospheric Chemistry and*
598 *Physics*, 17(2), pp.1227-1239.

599

600 IPCC, 2021: *Climate Change 2021: The Physical Science Basis. Contribution of Working Group I*
601 *to the Sixth Assessment Report of the Intergovernmental Panel on Climate Change*[Masson-
602 Delmotte, V., P. Zhai, A. Pirani, S.L. Connors, C. Péan, S. Berger, N. Caud, Y. Chen, L. Goldfarb,
603 M.I. Gomis, M. Huang, K. Leitzell, E. Lonnoy, J.B.R. Matthews, T.K. Maycock, T. Waterfield, O.
604 Yelekçi, R. Yu, and B. Zhou (eds.)]. Cambridge University Press, Cambridge, United Kingdom and
605 New York, NY, USA, In press, doi:[10.1017/9781009157896](https://doi.org/10.1017/9781009157896).

606

607 J. Muñoz-Sabater, Dutra, E., Agustí-Panareda, A., Albergel, C., Arduini, G., Balsamo, G.,
608 Boussetta, S., Choulga, M., Harrigan, S., Hersbach, H., Martens, B., Miralles, D. G., Piles, M.,
609 Rodríguez-Fernández, N. J., Zsoter, E., Buontempo, C., and Thépaut, J.-N.: ERA5-Land: A state-
610 of-the-art global reanalysis dataset for land applications, *Earth Syst. Sci. Data*,13, 4349–4383,
611 2021. <https://doi.org/10.5194/essd-13-4349-2021>.

612

613 Kochanov, R.V., Gordon, I.E., Rothman, L.S., Wcisło, P., Hill, C. and Wilzewski, J.S., 2016.
614 HITRAN Application Programming Interface (HAPI): A comprehensive approach to working with
615 spectroscopic data. *Journal of Quantitative Spectroscopy and Radiative Transfer*, 177, pp.15-30.

616



- 617 Lin, X., van der A, R., de Laat, J., Eskes, H., Chevallier, F., Ciais, P., Deng, Z., Geng, Y., Song, X.,
618 Ni, X. and Huo, D., 2023. Monitoring and quantifying CO₂ emissions of isolated power plants
619 from space. *EGUsphere*, pp.1-20.
620
- 621 Loizzo, R., Guarini, R., Longo, F., Scopa, T., Formaro, R., Facchinetti, C. and Varacalli, G., 2018,
622 July. PRISMA: The Italian hyperspectral mission. In *IGARSS 2018-2018 IEEE International
623 Geoscience and Remote Sensing Symposium* (pp. 175-178). IEEE.
624
- 625 Nassar, R., Hill, T.G., McLinden, C.A., Wunch, D., Jones, D.B. and Crisp, D., 2017. Quantifying
626 CO₂ emissions from individual power plants from space. *Geophysical Research Letters*, 44(19),
627 pp.10-045.
628
- 629 Nassar, R., Mastrogiacomo, J.P., Bateman-Hemphill, W., McCracken, C., MacDonald, C.G., Hill,
630 T., O'Dell, C.W., Kiel, M. and Crisp, D., 2021. Advances in quantifying power plant CO₂
631 emissions with OCO-2. *Remote Sensing of Environment*, 264, p.112579.
632
- 633 Nassar, R., Moeini, O., Mastrogiacomo, J.P., O'Dell, C.W., Nelson, R.R., Kiel, M., Chatterjee, A.,
634 Eldering, A. and Crisp, D., 2022. Tracking CO₂ emission reductions from space: A case study at
635 Europe's largest fossil fuel power plant. *Frontiers in Remote Sensing*, 3, p.98.
636
- 637 O'Dell, C.W., Connor, B., Bösch, H., O'Brien, D., Frankenberg, C., Castano, R., Christi, M.,
638 Eldering, D., Fisher, B., Gunson, M. and McDuffie, J., 2012. The ACOS CO₂ retrieval algorithm–



639 Part 1: Description and validation against synthetic observations. *Atmospheric Measurement*
640 *Techniques*, 5(1), pp.99-121.

641

642 O'Dell, C.W., Eldering, A., Wennberg, P.O., Crisp, D., Gunson, M.R., Fisher, B., Frankenberg, C.,
643 Kiel, M., Lindqvist, H., Mandrake, L. and Merrelli, A., 2018. Improved retrievals of carbon dioxide
644 from Orbiting Carbon Observatory-2 with the version 8 ACOS algorithm. *Atmospheric*
645 *Measurement Techniques*, 11(12), pp.6539-6576.

646

647 Rodgers, C.D., 2000. *Inverse methods for atmospheric sounding: theory and practice* (Vol. 2).
648 World scientific.

649

650 Reuter, M., Buchwitz, M., Schneising, O., Krautwurst, S., O'Dell, C.W., Richter, A., Bovensmann,
651 H. and Burrows, J.P., 2019. Towards monitoring localized CO₂ emissions from space: co-located
652 regional CO₂ and NO₂ enhancements observed by the OCO-2 and S5P satellites. *Atmospheric*
653 *Chemistry and Physics*, 19(14), pp.9371-9383.

654

655 Sierk, B., Bézy, J.L., Löscher, A. and Meijer, Y., 2019, July. The European CO₂ Monitoring
656 Mission: observing anthropogenic greenhouse gas emissions from space. In *International*
657 *Conference on Space Optics—ICSO 2018* (Vol. 11180, pp. 237-250). SPIE.

658

659 Taylor, T.E., O'Dell, C.W., Baker, D., Bruegge, C., Chang, A., Chapsky, L., Chatterjee, A., Cheng,
660 C., Chevallier, F., Crisp, D. and Dang, L., 2023. Evaluating the consistency between OCO-2 and



661 OCO-3 XCO₂ estimates derived from the NASA ACOS version 10 retrieval
662 algorithm. *Atmospheric Measurement Techniques Discussions*, 2023, pp.1-61.
663
664 Thorpe, A.K., Frankenberg, C., Thompson, D.R., Duren, R.M., Aubrey, A.D., Bue, B.D., Green,
665 R.O., Gerilowski, K., Krings, T., Borchardt, J. and Kort, E.A., 2017. Airborne DOAS retrievals of
666 methane, carbon dioxide, and water vapor concentrations at high spatial resolution: application to
667 AVIRIS-NG. *Atmospheric Measurement Techniques*, 10(10), pp.3833-3850.
668
669 Van Geffen, J., Boersma, K.F., Eskes, H., Sneep, M., Ter Linden, M., Zara, M. and Veefkind, J.P.,
670 2020. S5P TROPOMI NO₂ slant column retrieval: Method, stability, uncertainties and comparisons
671 with OMI. *Atmospheric Measurement Techniques*, 13(3), pp.1315-1335.
672
673 Varon, D.J., Jacob, D.J., McKeever, J., Jervis, D., Durak, B.O., Xia, Y. and Huang, Y., 2018.
674 Quantifying methane point sources from fine-scale satellite observations of atmospheric methane
675 plumes. *Atmospheric Measurement Techniques*, 11(10), pp.5673-5686.